Quantitative study of the photothermal properties of metallic nanowire networks.

Alan P. Bell [†§⊥], Jessamyn A. Farifield [†§⊥],Eoin K. McCarthy[§], Shaun Mills [†§⊥], John J. Boland [†§⊥], Guillaume Baffou[‖], and David McCloskey[‡§⊥]*

[†]School of Chemistry, Trinity College Dublin, Dublin 2, Ireland

[‡] School of Physics, Trinity College Dublin, Dublin 2, Ireland

[§] Centre for Research on Adaptive Nanostructures and Nanodevices (CRANN), Trinity College Dublin, Dublin 2, Ireland

[⊥] AMBER Research Centre, Trinity College Dublin, Dublin 2, Ireland

[‖] Institut Fresnel, CNRS, Aix Marseille Université, Centrale Marseille, UMR 7249, 13013 Marseille, France

KEYWORDS Thermoplasmonics, nanowire networks, wave-front sensing, nano-welding

ABSTRACT

We quantitatively measure the local steady state temperature increase, heat source density and absorption in Ag, Au and Ni metallic nanowire networks under optical illumination. We demonstrate direct experimental confirmation of increased heat generation at the junction between two metallic nanowires, and stacking dependent absorption of polarized light. Due to co-operative thermal effects, the local temperature distribution in a network is shown to be completely delocalized on a micrometer scale, despite the nanoscale features in the heat source density. The steady state temperature rise is shown to scale linearly with the illumination diameter allowing calibration of the local temperature field. The total illumination area is thus identified as an important parameter controlling local temperature rise, often not considered in thermoplasmonic experiments. Comparison of the experimental temperature profile with numerical simulation allows an upper limit for the effective thermal conductivity of an Ag nanowire network to be established at 43 $Wm^{-1}K^{-1}$ (0.1 κ_{bulk}).

TEXT

Photothermal properties of plasmonic nanoparticles have generated much interest over the last decade, resulting in the development of many novel techniques and technologies including photothermal cancer therapy[1-3], photoacoustic tomography[4], local drug release[5], nanosurgery[6-7], microfluidics[8], manipulation of cell adhesion[9], local superheating[10] and heat assisted magnetic recording[11]. Many nanoparticles of various compositions, morphologies and sizes have been investigated in order to estimate and compare their capabilities as efficient nanoscale sources of heat under illumination. While spherical gold nanoparticles are best suited for applications under visible illumination (unless agglomerated)[12], gold nanoshells[13-14] and nanorods[15] are excellent candidates for biomedical applications due to their tunable near infrared plasmonic resonance lying within a transparency window of biological tissue.

Despite studies of a wide variety of plasmonic nanoparticles, the photothermal properties of metallic nanowires has not been so widely investigated. Chemically synthetized nanowires can be mass produced and have an extremely large aspect ratio and surface to volume ratio, which is expected to yield singular thermal properties. Large quantities of these nanowires can be easily deposited on a surface using spray deposition or spin coating techniques[16]. The resulting nanowire networks exhibit specific electrical [17-19], optical[20] and physical[21] properties, which are in general controlled by the properties of the constituent junctions. Nanowire networks can be used to fabricate transparent flexible conductors , strain sensors [12] self-healing materials[22], improved solar cells[23], and artificial skin[24-25].

Nanowire networks can be considered as a random ensemble of individual nanoparticles or as an effective film with considerable reduced thermal conductivity. Ensembles or networks of plasmonic structures lead to collective heating effects which result in two distinct regimes, where the temperature increase is either localized around each nanoparticle, or completely delocalized across the array[26]. Indeed, thermoplasmonic related experiments very rarely concern single nanoparticle heating and heating many nanoparticles at a time can lead to unexpected temperature profiles in the surrounding medium[27].

In this article, we present a comprehensive investigation of the photothermal properties of plasmonic nanowire networks. To fully understand heating in such systems we initially focus on the simple case of isolated metallic nanowires, made of gold, silver and nickel and detail their polarization dependent absorption. Subsequently, we investigate heat generation and temperature confinement at discrete nanowire junctions and their stacking dependent absorption. Finally, we investigate complex networks of randomly orientated connected nanowires and discuss delocalization and scaling of the local temperature distribution.

Electromagnetically induced heating in metals is predominantly the result of Joule effect. This process is proportional to square of the electric field inside the metal and the intrinsic

material losses of the metal. In a general form, the volumetric heat source density $q(\mathbf{r})$ [W/m^3] generated inside the metal is given by [28]

$$q(\mathbf{r}) = (n^2\omega/2)\,\mathrm{Im}(\varepsilon)\left|\mathbf{E}(\mathbf{r})\right|^2 \qquad (1)$$

where n is the refractive index of the surrounding medium, ω is the angular frequency of the incident light, ε is the frequency dependent permittivity of the metal, which determines the local response of the electrons to the external field and **E** is the electric field. All of the material loss mechanisms, including interband transitions, are contained within the imaginary component of the permittivity. The total power absorbed by a nanoparticle P_{abs} [W], is then given by the integral of the volumetric heat source density over the volume of the particle

$$P_{abs} = \int_{NW} q(\mathbf{r})d\mathbf{r}\,. \qquad (2)$$

Under optical illumination the metallic nanoparticle will thermally equilibrate internally on a fast timescale which depends on particle size, and reach a stable thermal equilibrium with the surrounding medium on a longer timescale determined by the thermal diffusivity of the surrounding media. Typical timescales for a nanoparticle in water are on the order of nanosecond for internal thermal equilibrium and microseconds for equilibrium with surrounding media[29]. Under illumination and in the steady state, the inner nanoparticle temperature distribution $T(\mathbf{r})$ is governed by the Poisson equation

$$\kappa\nabla^2 T(\mathbf{r}) = -q(\mathbf{r})\,, \quad (3)$$

where κ is the thermal conductivity of the metal, and $q(\mathbf{r})$ is the volumetric heat source density in the nanowire. Outside the nanoparticle the temperature distribution is governed by the Laplace equation:

$$\nabla^2 T(\mathbf{r}) = 0\,, \qquad (4)$$

If the heat source density *q(**r**)* is known, the steady state temperature rise $\delta T(\mathbf{r})$ for an arbitrarily shaped heat source can then be described as a convolution of *q(**r**)* with the Green's function G_T for the Laplace equation as

$$\delta T(\mathbf{r}) = \int q(\mathbf{r_i}) G_T(\mathbf{r}, \mathbf{r_i}).d\mathbf{r_i} \text{ , (5)}$$

where *q(**r**)* is the heat source density defined in *eq.1* and $G_T(\mathbf{r}, \mathbf{r_i}) = \frac{1}{4\pi\kappa_m}\frac{1}{|\mathbf{r}-\mathbf{r_i}|}$ is the Green's function for the Laplace equation[30], and κ_m is the thermal conductivity of the surrounding medium. This Greens function approach is advantageous, as only the region of the heat source needs to be meshed, and more importantly, if the steady state temperature distribution is measured, the heat source density can be retrieved using a deconvolution algorithm.

The experimental local steady state temperature measurements were performed using a recently developed technique named TIQSI for thermal imaging using quadriwave shearing interferometry[31]. In brief, the samples are immersed in glycerol, and a plane wave crosses the region of interest undergoing a distortion due to the thermally induced variation of the refractive index in the glycerol. This wavefront distortion is imaged using a QSI wavefront sensor and then processed using an inversion algorithm to retrieve both the local temperature increase (δT [K]) and the 2D heat source density (p [μW/μm^2]) with sub-micrometric spatial resolution (~400 nm). The 2D heat source density *p(x,y)* measured with this technique is defined as the integral of the 3D heat source density q over the thickness of the wire. Interestingly, integration of the experimental maps of *p(x,y)* over x and y allows quantitative measurement of the total power absorbed (or equivalently delivered) by the composite nanoparticle[32]. Dividing this integral by the incident irradiance I_0 gives an expression for absorption cross section $\sigma_{abs}[m^2]$, which is common metric to define the absorption strength of a nanoparticle

$$\sigma_{abs} = \frac{1}{I_0}\int p(x,y)dxdy\,. \quad (6)$$

TIQSI therefore provides a powerful non-invasive technique to recover the local steady state temperature increase, the heat source density, and the absorption cross sections of nanoscale particles with arbitrary geometry, like the complex nanowire system investigated herein.

Experimental samples were formed by spray deposition of commercially available single crystalline gold (Sigma Aldrich), silver (Seashell Technology) and nickel (Nanomaterials.it) nanowires onto quartz substrates. The density of the nanowire distribution was controlled to either have a predominance of single nanowires, isolated nanowire junctions/crossings, or fully connected nanowire films. The Au nanowires have a passivation monolayer of cetyltrimethylammonium bromide (CTAB) to avoid aggregation in solution, whereas the Ag nanowires have a 3 nm thick dielectric surface coating of poly(vinylpyrrolidone) (PVP). The Ni wires have a 5 nm surface oxide layer. Statistical analysis of TEM and SEM imaging confirmed an average diameter D (length L) of 50 nm (8 μm) for the Au nanowires, 90 nm (7.3 μm) for Ag, and 80 nm (9.4 μm) for Ni (see supplemental *Fig.S1*).

Initially we investigated heating in single isolated Au, Ag and Ni nanowires. These nanowires show a strong frequency and polarization dependent absorption due to the excitation of localized surface plasmons (LSP) transverse to the wire axis (*Fig.S2*). Without loss of generality we can consider two cases, depicted in *Fig.1a*, of incident light linearly polarized along the nanowire axis, referred to as the transverse magnetic case (*TM*), and light polarized perpendicular to the axis, referred to as the transverse electric case (*TE*). The response for arbitrary incident polarization can be calculated as a linear combination of these two cases. The finite element method (FEM) is employed to numerically calculate the internal electric field in the nanowire under optical illumination, which is then converted to the heat source density using *eq.1*. *Figure.1b* shows the heat source density distribution for a 60 nm diameter Au nanowire illuminated with a free space wavelength of 532 nm. The effect of the LSP is to

increase the internal field penetration and therefore the heat generation at the resonant frequency for the TE polarized case and not for the TM case. Experimental heating measurements were performed using a 532 nm diode pumped solid state laser (10 W Millenia, SpectraPhysics) as the thermal excitation source. The laser was expanded onto a variable iris in the image plane of the objective to produce a top hat intensity distribution on the sample over a 10.2 μm diameter area. The laser power was then varied to control the incident irradiance. *Figure 1c* shows an optical image of a single Au nanowire 10 μm in length. The nanowire appears dark in transmission and is quite visible despite nanoscale lateral dimensions due to its large scattering and absorption cross section and blurring from the diffraction limit of the collection objective (NA=1.4). The excitation area is shown as a white dashed line. *Figure 1d* shows the measured steady state temperature distribution with incident irradiance I_0 = 2.82 mW/μm^2 for *TE* incident polarization. This intensity is sufficient to induce significant heating in the nanowire leading to a temperature increase of 200 K. The 2D heat source density (p [μW/μm^2]) distribution can be extracted (*Fig.1e*), showing as expected that the heat is delivered uniformly along the length of the nanowire. Integration of this heat source density in accordance with *eq.6* gives an absorption cross section for the nanowire of $\sigma_{abs}^{TE} = 0.71\mu m^2$ for TE polarization compared to $\sigma_{abs}^{TM} = 0.35\mu m^2$ for TM polarization.

To experimentally quantify the polarization dependent absorption in the nanowires the ratio of the steady state temperatures under fixed excitation intensity for TE and TM illumination was measured for a range of distinct nanowires. At an excitation wavelength of 532 nm the Au nanowires show the most anisotropy due to the frequency dependence of the LSP resonance, with a ratio $R = \sigma_{abs}^{TE} / \sigma_{abs}^{TM}$ of 3, Ag has R=1.5 and Ni has R=1. The wavelength dependence of this ratio calculated from Mie theory for an infinite cylinder is plotted in *Fig. S3*. *Figure. 1f* compares experimental values of R (columns) for three different Au, Ag and Ni nanowires with the calculated ratios from the Mie theory solution (solid lines). Single metallic nanowires can

159 also support propagating surface plasmon polariton (SPP) modes, which can be excited at a
160 discontinuity such as the finite end of the nanowire, allowing their use as nanoscale waveguides
161 [33]. To study the contribution of these SPP modes to the total absorption cross section we
162 conducted 3D FEM simulations. The intensity enhancement *Fig.S3a* and heat source density
163 *Fig.S2c* for a 30 nm radius infinite Ag wire, are compared with that of a semi-infinite wire with
164 a 30 nm radius spherical capped *Fig.S3c,d*. The relative heat source density is normalized to
165 Mie theory for an infinite wire shows that the launched SPP modes contribute to increased
166 heating in only the first 250 nm of the wire. The wire is in a symmetric environment (glycerol
167 and glass with similar refractive index), so it is difficult to efficiently match the momentum
168 required to launch a bound SPP mode in the nanowire. This sharp 250 nm falloff can be
169 attributed to launching of lossy modes in the wire. The total contribution of SPPs to the
170 absorption cross section can be seen by plotting the cumulative difference of the heating in the
171 finite wire to that in an infinite in *Fig. S3f,* and is less than 7% for a 1 μm long wire. The
172 agreement of the ratio of measured absorption cross sections with Mie theory, which is for an
173 infinitely long nanowire, demonstrates that although it is possible to excite SPPs at the
174 nanowire ends, they do not contribute significantly to the polarization response of heat
175 generation.

176 A cross section of the steady state temperature distribution through the center of an Au
177 nanowire perpendicular to the nanowire axis is shown in *Fig.1g* for *TE* (green dots) and *TM*
178 (red dots) illumination. For a wire with uniform volumetric heat source density, the temperature
179 distribution shows an ln(r) dependence close to the nanowire as expected from an infinite wire,
180 and a 1/r dependence at further distances due to its finite length. The solid line in *Fig.1g* shows
181 the temperature profile is well fitted with logarithmic falloff in the first 5 μm with a 1/r
182 dependence afterwards. This demonstrates that a single nanowire can create a temperature
183 increase which is localized to a full width half maximum (FWHM) of 2.2 μm in the glycerol,

with a thermal gradient (which depends on incident power) of the order 95 K/μm. Measurements of temperature distributions and heat source densities were taken for multiple nanowires and junctions on each sample. For brevity only a few selected results were shown in the main text, however given the speed and simplicity of the technique a large number of nanowire samples were investigated. Experimental results over a larger sample set of single nanowires are displayed in the supplemental information (*Fig. S4*).

Subsequently we investigated the more complex case of heating at the junction between two nanowires. Recent experimental studies have shown that optical illumination of nanowire networks can significantly increase the film conductivity by induced re-crystallization at nanowire junctions referred to as "nano-welding"[34-35]. This effect was postulated to be due to enhanced electric fields and heating at nanowire junctions, however only a numerical investigation of the detailed mechanism was possible[28]. In this work we quantitatively measure the heat source density at a junction between two nanowires and directly evidence enhanced heating. Single nanowire junctions of Au, Ag, and Ni were investigated for two orthogonal cases of incident polarization. An optical image of the junction and illuminated area and the 2D heat source density maps for two orthogonal polarizations are displayed in *Fig. 2a, b* and *c*, for Au, Ag and Ni, respectively. The results clearly demonstrate a localized hot spot in the heat source density at the intersection for the nanowires for all three metals. The polarization dependence shows a distinct asymmetry in that one nanowire will contribute significantly more to the heating for a particular incident polarization, which is most evident in the case of the Au nanowires with excitation wavelength of 532 nm. The experimentally mapped 2D heat source density is numerically integrated to attain the total absorption cross-section of the nanowire junction. To accurately determine this value the integration is performed radially starting from the geometric center of the illuminated area. The cumulative integration is shown as a function

of radius in *Fig. 2d*. The total absorption cross section is then determined as the value at which the cumulative integration levels off. In the case of the Au nanowire junction shown in *Fig.2a* integration of the experimentally mapped 2D heat source density *p* yields an absorption cross section of σ_{abs}= 1.15±0.02 μm^2, which is only marginally larger than that of two isolated nanowires (σ_{abs}^{TE}= 0.71±0.02 μm^2, σ_{abs}^{TM}=0.35±0.02 μm^2) due to heat source density enhancement at the junction. The two intersecting nanowires can be thought of as a composite nanoparticle, which has increased absorption cross section from a single nanowire[36]. *Fig.2e* shows that the temperature rise of 120 K can be reached at a Ni nanowire junction with an irradiance of 1.32 mW/μm^2. The spreading of the temperature distribution compared to the heat source density depends on the thermal conductivity of the surrounding medium. For completeness a wider selection of thermal maps related to various nanowire configurations are presented in supplementary information (*Fig. S5*).

The polarization dependence of the heat source density of the nanowire junctions can be explained by considering the stacking of the nanowires. We can identify two cases as depicted in *Fig.3*; Case 1 where the incident polarization is perpendicular (*TE*) to the top nanowire and Case 2 where the incident polarization is along the axis (*TM*) of the top nanowire. We use three dimensional finite element method (FEM) simulation to examine the local electric field enhancement and the resistive heating profiles. *Figure.3* shows the case of 532 nm light incident on 60 nm diameter Ni nanowires with a 4 nm gap between wires at the junction, to account for the surface oxide. For both cases there is an enhancement in the electric field at the gap between the two wires. This electric field enhancement leads to an increase of the electric field inside the nanowires at the junction, which in turn leads to enhanced localized heating. The maximum contrast is achieved for Case 1 where the incident polarization is perpendicular to the top nanowire axis. In this case a LSP is effectively excited in the top nanowire resulting in a field enhancement of 9.5 times at the junction (*Fig.3b,c*). For Case 2 the top nanowire

scatters the incident light which reduces the LSP effect in the bottom nanowire leading to a smaller field enhancement of 3.5 times and less contrast in the heating profile (*Fig.3f,g*).

The 2D heat source density profile is calculated from the FEM results by integrating the 3D heat source density over the z axis. The simulation domain for the FEM was limited to 1 um by 0.5 μm by 0.5 μm due to finite computational resources. It is not feasible to simulate the full 10.2 μm using this method, so periodic boundary conditions were used in the x-y directions, with perfectly matched layers in the z direction. The FEM determined 2D heat source density shows the expected enhanced heat generation at the nanowire junction, however the absolute value of the 2D heat source density cannot be directly compared with the longer experimentally measured nanowires of *Fig.2*. The experimental results are also convolved with the point spread function of the collection objective. SPPs excited at this junction may provide an additional absorption mechanism to increase the absorption cross section of the composite particle, but this effect will be included in the experimentally measured cross sections and FEM simulations. In both excitation cases larger heating is observed in the *TE* illuminated nanowire consistent with previous predictions in silver nanowires[18]. The stacking dependence of the heat source density in the FEM simulations explains the polarization dependence observed in the experimental measurements.

Finally we investigated heating in large scale fully connected nanowire networks which are physically relevant for applications such as transparent conductors, flexible electronics and memristive devices. Nanowire networks can be considered as an ensemble of individual nanowires, or as a thin film with considerably reduced effective thermal conductivity. Studies on heating in ensembles of nanoparticles reveal that the steady state temperature distribution can be strongly localized around each nanoparticle, or conversely, completely uniform throughout the system, depending on nanoparticle coverage[37, 38] on the substrate.

To quantitatively investigate the local temperature increase in nanowire network systems we map the temperature distribution of an Ag nanowire network under different optical excitation conditions. A 40× objective and a variable aperture were employed to achieve illumination of the network over two distinct circular areas with diameters of D=50 μm and D=100 μm. Scattered light optical images are shown in *Fig.4a,b*, with the illumination area identified using a white circle. The laser power was controlled to maintain constant intensity on the sample $I = 0.127 mW/\mu m^2$ (*Fig.4b,c*). Profiles of the local temperature along a line through the center of the illumined area are shown in Fig. 4d. The experimental temperature maps (*Fig.4 c,d*) and profiles (*Fig.4e*) demonstrate that at nanowire density physically relevant for transparent conductors the temperature increase is fully delocalized on the micrometric scale throughout network despite a contrasted heat source density on the nanoscale. The total power absorbed in the network can be found by integrating the heat source density. We find that the silver nanowire network absorbs only a small fraction, 0.4% of the incident power, at this network density and wavelength. This is 10% of the power that would be absorbed by a 60 nm thick continuous Ag film. Note that TIQSI allows a quantitative measurement of absorbed power, not an approximate absorption measurement by transmission measurement.

In contrast to the steady state temperature surrounding a finite collection of nanoparticles, the local temperature reached of a thin film depends on the thermal conductivity of the film. A high thermal conductivity will spread the energy resulting in a lower steady state temperature increase in the center of the illumination area and a smaller temperature gradient (*Fig.S6*). Using the experimentally measured absorbed power as a source term for a 3D FEM thermal simulation we find that in order to match experimental results, we must use a thin film thermal conductivity less than 43 $Wm^{-1}K^{-1}$, which is 10% that of a bulk silver film (429 $Wm^{-1}K^{-1}$). This is defined as an upper limit for the thermal conductivity of the effective film, as the dependence of the steady state temperature distribution ceases when the thermal conductivity of the film is

283 less than the surrounding media (*Fig.S6*). The dashed lines in *Fig.5e* show the FEM results
284 with the effective thin film thermal conductivity. Deviations from the ideal case are due to
285 density variations in the network which correlate well with the images in *Fig.4a,b*.
286 The delocalization of temperature across the nanowire network has important implications
287 for controlling the local steady state temperature rise under optical illumination. Experimental
288 measurements were performed at different incident powers and illumination areas (*Fig. S6*).
289 The maximum temperature increase T_0 is shown to scale linearly with the diameter of the
290 illuminated D area according to $T_0 \propto DI$ or equivalently $T \propto P/D$. This is what would be
291 expected for a 2D circular heat source[26]. This important fact means that to appropriately scale
292 the incident power to maintain a constant temperature at the interface, the illuminated area
293 needs to be considered. To illustrate this fact the isotherms of local temperature are plotted
294 over the incident power and illumination area parameter space in *Fig.4g*. Using this
295 experimental calibration we can now know the local steady state temperature for any incident
296 power and illumination area (accounting for density variations in the network). This is an
297 important calibration as the local temperature rise is needed in order to make quantitative
298 comparisons between the efficacy of thermally (hot-plate)[37], electrically[38] and optically[35]
299 induced increase of conductivity in nanowire transparent conductors. We show that both the
300 incident power and illumination area are required to determine the actual temperature at the
301 sample. Specification of the size of the illuminated area is often omitted in reported
302 experimental studies in thermoplasmonics.
303 In conclusion, we directly measure the optically induced local temperature rise, heat source
304 density and absorption cross sections in nanowire systems of varying complexity. We directly
305 evidence enhanced heat generation at the junction between two single nanowires, an effect
306 which previously has only been postulated numerically. We show that this temperature
307 localization exists even for nickel nanowires, which have a strongly damped plasmonic

resonance. The polarization dependence of heating in single nanowire junction is explained as resulting from the stacking order. The temperature distribution in an Ag nanowire network is shown to be delocalized and scale linearly with the diameter of the illuminated region. From this scaling we can calibrate the local temperature rise at the surface for different powers and illumination areas. Due to collective heating of the nanowires we show that it is imperative to consider the illuminated area in order to accurately determine the local steady state temperature reached. An upper limit for the effective thermal conductivity of an Ag nanowire network is given as 43 $Wm^{-1}K^{-1}$ by comparison of the steady state temperature profile with numerical FEM simulations. This work provides quantitative measurements to aid in interpretation of thermally induced effects in nanowire systems such as nano-welding for transparent conductors and nanowire networks, filament formation in nickel nanowire networks[39] and film heaters[40]. Previous studies were unable to quantitatively measure optically induced local temperature increase, making comparison between optically induced heating and thermally induced heating (hotplate) qualitative. This work contributes to understanding heat generation and dissipation in nanoscale systems, which is of major importance for further scaling of electronic devices and development of new nanotechnologies.

Supporting Information Available: Supplementary information contains TEM images and statistical analysis of diameter and length distributions of nanowires used. Further experimental results are provided. This material is available free of charge via the Internet at http://pubs.acs.org.

FIGURES (Word Style "VA_Figure_Caption").

TOC figure

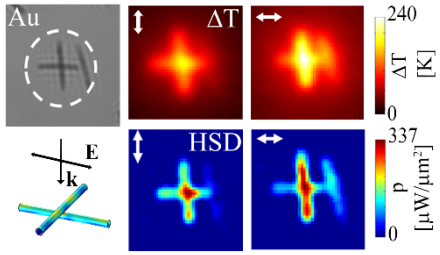

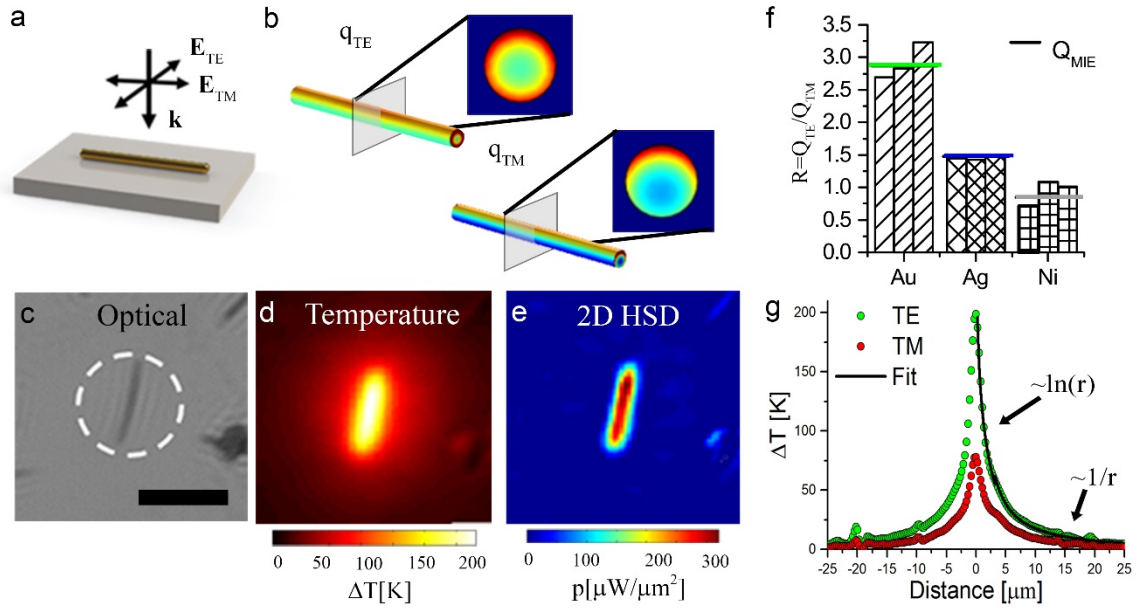

Figure 1. (a) Schematic of Transverse Electric (TE) and Transverse Magnetic (TM) cases of incident excitation for a single nanowire. (b) Numerically calculated volumetric heat source density distribution *q(**r**)* for TE and TM cases on single Au nanowire of diameter 60 nm. (c) Optical image in transmission of a single Au nanowire. Dashed circle shows the illumination area. Scale bar 10 μm. (d) Experimentally measured steady state temperature distribution under illumination intensity of I_0= 2.82 mW/μm^2. (e) Experimentally measured 2D heat source density distribution *p(**r**)*. (f) Ratio of heating $R = \sigma_{abs}^{TE} / \sigma_{abs}^{TM}$ for TE and TM cases. Columns represent experimental measurements on three distinct nanowires. The solid lines are the predicted ratios from Mie theory. (g) Cross section of experimentally measured temperature distribution for TE and TM incident polarization. The temperature distribution shows an ln(r)

dependence close to the nanowire as expected from an infinite wire, and a 1/r dependence at further distances due to its finite length.

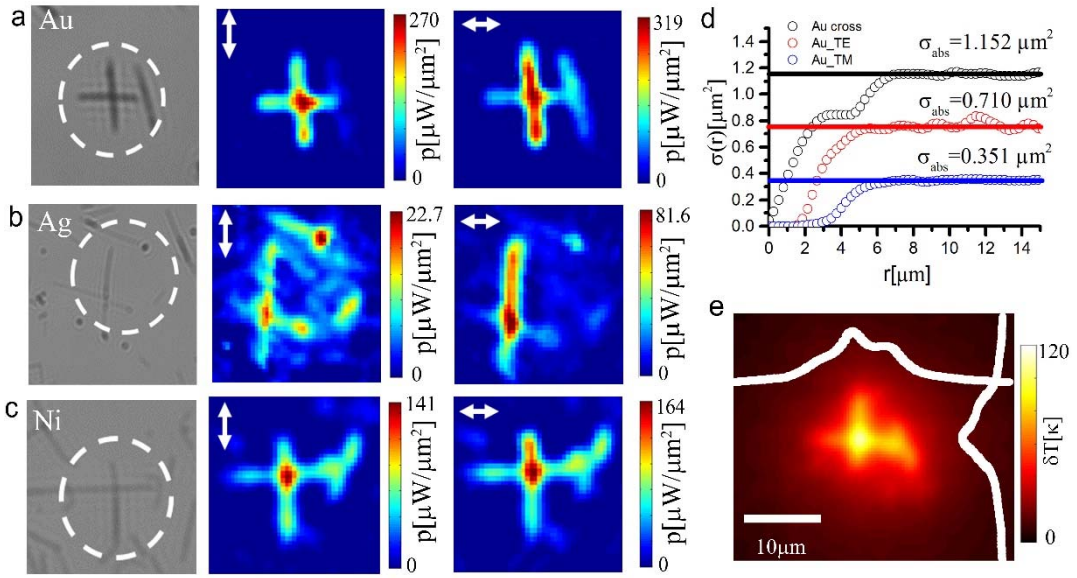

Figure 2. Optical images and heat source density maps *p* for different incident polarizations on single nanowire junctions for (a) Au (b) Ag and (c) Ni nanowires. (d) Integrating the 2D heat source densities radially from the center point of the junction allows quantitative measurement of the absorption cross section. Plotted is the cumulative integral for the Au cross in (a) compared a single Au wire under TE and TM polarization. (e) Temperature map for the Ni nanowire junction from (c) with incident light polarized along x-axis. The spreading of the temperature profile is determined by the thermal conductivity of the surrounding media. Overlays show cross sections of temperature profile through center of junction.

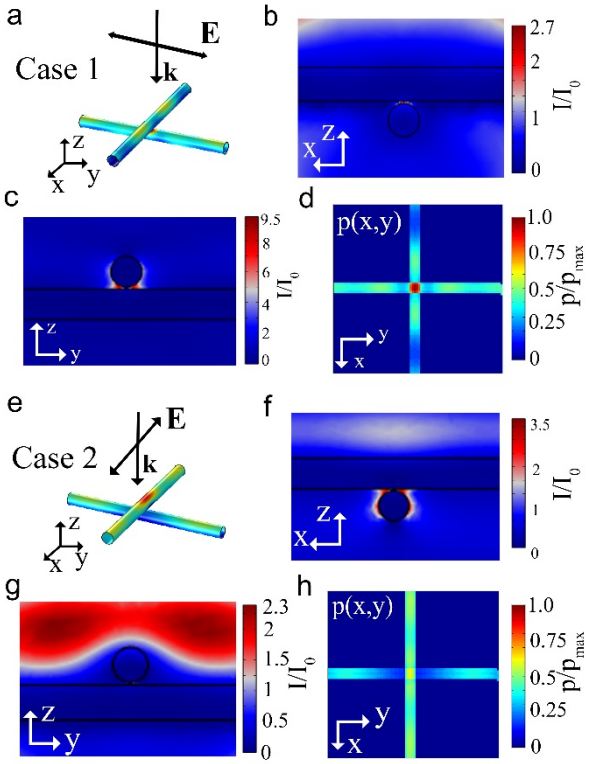

Figure 3. (a) 3D map of resistive heating distribution in Ni nanowire junction calculated from FEM. Incident illumination is polarized perpendicular to the top nanowire; termed Case1. (b) Intensity enhancement in the z-x plane through center of junction. (c) Intensity enhancement in the z-y plane. (d) 2D heat source density map obtained from integrating 3D results along z axis. (e)-(h) Same as (a)-(d) but incident light is polarized along the axis of the top nanowire; termed Case 2.

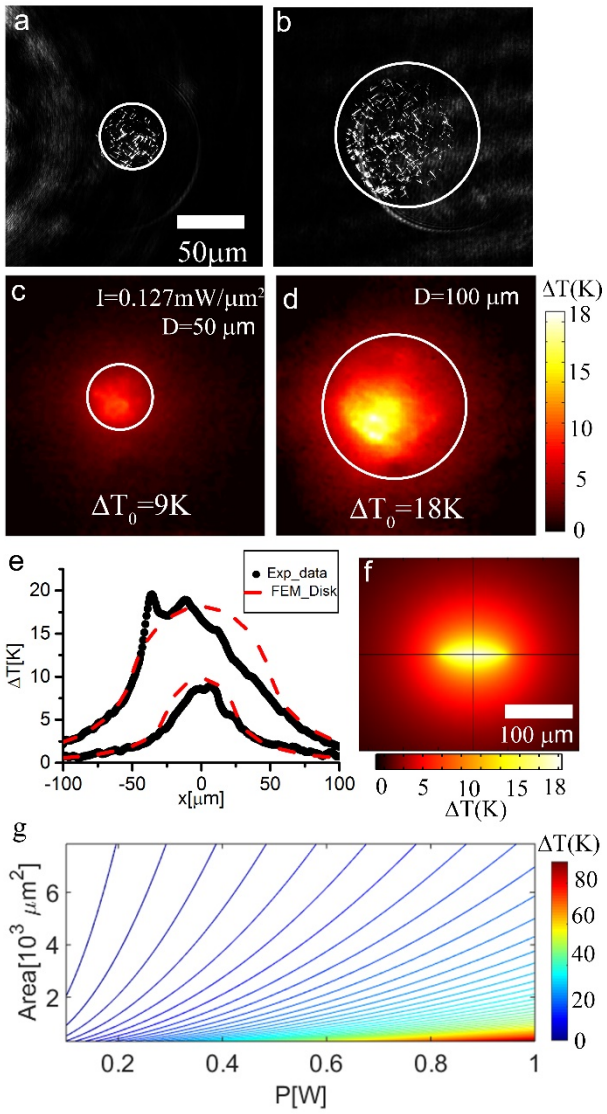

370

371 **Figure 4.** Scattered light images of the excitation laser depicting the illuminated areas of
372 diameter (a) D=50 μm and (b) D=100 μm. (c),(d) Experimental temperature maps taken at
373 constant irradiance (e) Cross section of temperature map through center of illumination region.
374 Dashed red lines show FEM simulation of the temperature distribution. (f) Out of plane
375 temperature map calculated from 3D FEM. (g) Contour plot of isotherms in the incident power,
376 illumination area parameter space. Results show careful consideration of both incident power
377 and illumination area required to accurately determine the local temperature increase.

378

AUTHOR INFORMATION

Corresponding Author

*Email: mccloskd@tcd.ie

Author Contributions

A.P.B and D.M.C performed the experimental measurements. J.A.F and J.F.B provided nanowire samples and expertise on nanowire systems. E.K.M.C and S.M. performed TEM measurements and statistical analysis of nanowire dimensions. G.B. developed the experimental technique and provided expertise on Thermoplasmonics. D.M.C. designed and performed the experiments, devised analytical and numerical models, coordinated and drafted the work. The manuscript was written through contributions of all authors. All authors have given approval to the final version of the manuscript.

ACKNOWLEDGMENT

The authors wish to acknowledge funding from the European Research Council under Advanced Grant 321160. This publication has emanated from research supported in part by a research grant from Science Foundation Ireland (SFI) under Grant Number SFI/12/RC/2278. J.A.F. acknowledges funding from the Irish Research Council EMPOWER Fellowship. The travel in this work was made possible through the Irish Research Council ULYSSES travel grant: award number 12678. G.B. acknowledges financial support from the Agence Nationale de la Recherche (ANR) grant NATO (ANR-13-BS10-0013).

REFERENCES

1. Ayala-Orozco, C.; Urban, C.; Bishnoi, S.; Urban, A.; Charron, H.; Mitchell, T.; Shea, M.; Nanda, S.; Schiff, R.; Halas, N.; Joshi, A., Sub-100 nm gold nanomatryoshkas improve photo-thermal therapy efficacy in large and highly aggressive triple negative breast tumors. *Journal of Controlled Release* **2014,** *191* (0), 90-97.
2. Ayala-Orozco, C.; Urban, C.; Knight, M. W.; Urban, A. S.; Neumann, O.; Bishnoi, S. W.; Mukherjee, S.; Goodman, A. M.; Charron, H.; Mitchell, T.; Shea, M.; Roy, R.; Nanda, S.; Schiff, R.; Halas, N. J.; Joshi, A., Au Nanomatryoshkas as Efficient Near-Infrared Photothermal Transducers for Cancer Treatment: Benchmarking against Nanoshells. *ACS Nano* **2014,** *8* (6), 6372-6381.
3. Gobin, A. M.; Lee, M. H.; Halas, N. J.; James, W. D.; Drezek, R. A.; West, J. L., Near-Infrared Resonant Nanoshells for Combined Optical Imaging and Photothermal Cancer Therapy. *Nano Letters* **2007,** *7* (7), 1929-1934.
4. Wang, L. V.; Hu, S., Photoacoustic Tomography: In Vivo Imaging from Organelles to Organs. *Science (New York, N.y.)* **2012,** *335* (6075), 1458-1462.
5. Han, G.; Ghosh, P.; De, M.; Rotello, V. M., Drug and gene delivery using gold nanoparticles. *Nanobiotechnol* **2007,** *3* (1), 40-45.
6. Huschka, R.; Barhoumi, A.; Liu, Q.; Roth, J. A.; Ji, L.; Halas, N. J., Gene Silencing by Gold Nanoshell-Mediated Delivery and Laser-Triggered Release of Antisense Oligonucleotide and siRNA. *ACS Nano* **2012,** *6* (9), 7681-7691.
7. Urban, A. S.; Pfeiffer, T.; Fedoruk, M.; Lutich, A. A.; Feldmann, J., Single-Step Injection of Gold Nanoparticles through Phospholipid Membranes. *ACS Nano* **2011,** *5* (5), 3585-3590.
8. Donner, J. S.; Baffou, G.; McCloskey, D.; Quidant, R., Plasmon-Assisted Optofluidics. *ACS Nano* **2011,** *5* (7), 5457-5462.
9. Zhu, M.; Baffou, G.; Meyerbröker, N.; Polleux, J., Micropatterning Thermoplasmonic Gold Nanoarrays To Manipulate Cell Adhesion. *ACS Nano* **2012,** *6* (8), 7227-7233.
10. Baffou, G.; Polleux, J.; Rigneault, H.; Monneret, S., Super-Heating and Micro-Bubble Generation around Plasmonic Nanoparticles under cw Illumination. *The Journal of Physical Chemistry C* **2014,** *118* (9), 4890-4898.
11. Challener, W. A.; Peng, C.; Itagi, A. V.; KarnsD; Peng, W.; Peng, Y.; Yang, X.; Zhu, X.; Gokemeijer, N. J.; Hsia, Y. T.; JuG; Rottmayer, R. E.; Seigler, M. A.; Gage, E. C., Heat-assisted magnetic recording by a near-field transducer with efficient optical energy transfer. *Nat Photon* **2009,** *3* (4), 220-224.
12. Hutter, E.; Fendler, J. H., Exploitation of Localized Surface Plasmon Resonance. *Advanced Materials* **2004,** *16* (19), 1685-1706.
13. Prodan, E.; Radloff, C.; Halas, N. J.; Nordlander, P., A Hybridization Model for the Plasmon Response of Complex Nanostructures. *Science* **2003,** *302* (5644), 419-422.
14. Cole, J. R.; Mirin, N. A.; Knight, M. W.; Goodrich, G. P.; Halas, N. J., Photothermal Efficiencies of Nanoshells and Nanorods for Clinical Therapeutic Applications. *The Journal of Physical Chemistry C* **2009,** *113* (28), 12090-12094.
15. Link, S.; El-Sayed, M. A., Spectral Properties and Relaxation Dynamics of Surface Plasmon Electronic Oscillations in Gold and Silver Nanodots and Nanorods. *The Journal of Physical Chemistry B* **1999,** *103* (40), 8410-8426.
16. Scardaci, V.; Coull, R.; Lyons, P. E.; Rickard, D.; Coleman, J. N., Spray Deposition of Highly Transparent, Low-Resistance Networks of Silver Nanowires over Large Areas. *Small* **2011,** *7* (18), 2621-2628.

17. Bellew, A. T.; Bell, A. P.; McCarthy, E. K.; Fairfield, J. A.; Boland, J. J., Programmability of nanowire networks. *Nanoscale* **2014,** *6* (16), 9632-9639.
18. Fairfield, J. A.; Ritter, C.; Bellew, A. T.; McCarthy, E. K.; Ferreira, M. S.; Boland, J. J., Effective Electrode Length Enhances Electrical Activation of Nanowire Networks: Experiment and Simulation. *ACS Nano* **2014,** *8* (9), 9542-9549.
19. Nirmalraj, P. N.; Bellew, A. T.; Bell, A. P.; Fairfield, J. A.; McCarthy, E. K.; O'Kelly, C.; Pereira, L. F. C.; Sorel, S.; Morosan, D.; Coleman, J. N.; Ferreira, M. S.; Boland, J. J., Manipulating Connectivity and Electrical Conductivity in Metallic Nanowire Networks. *Nano Letters* **2012,** *12* (11), 5966-5971.
20. Chen, R.; Das, S. R.; Jeong, C.; Khan, M. R.; Janes, D. B.; Alam, M. A., Co-Percolating Graphene-Wrapped Silver Nanowire Network for High Performance, Highly Stable, Transparent Conducting Electrodes. *Advanced Functional Materials* **2013,** *23* (41), 5150-5158.
21. McCarthy, E. K.; Bellew, A. T.; Sader, J. E.; Boland, J. J., Poisson's ratio of individual metal nanowires. *Nat Commun* **2014,** *5*.
22. Gong, C.; Liang, J.; Hu, W.; Niu, X.; Ma, S.; Hahn, H. T.; Pei, Q., A Healable, Semitransparent Silver Nanowire-Polymer Composite Conductor. *Advanced Materials* **2013,** *25* (30), 4186-4191.
23. Langley, D. P.; Giusti, G.; Lagrange, M.; Collins, R.; Jiménez, C.; Bréchet, Y.; Bellet, D., Silver nanowire networks: Physical properties and potential integration in solar cells. *Solar Energy Materials and Solar Cells* **2014,** *125* (0), 318-324.
24. Boland, J. J., Flexible electronics: Within touch of artificial skin. *Nat Mater* **2010,** *9* (10), 790-792.
25. Takei, K.; Takahashi, T.; Ho, J. C.; Ko, H.; Gillies, A. G.; Leu, P. W.; Fearing, R. S.; Javey, A., Nanowire active-matrix circuitry for low-voltage macroscale artificial skin. *Nat Mater* **2010,** *9* (10), 821-826.
26. Baffou, G.; Berto, P.; Bermúdez Ureña, E.; Quidant, R.; Monneret, S.; Polleux, J.; Rigneault, H., Photoinduced Heating of Nanoparticle Arrays. *ACS Nano* **2013,** *7* (8), 6478-6488.
27. Baffou, G.; Urena, E. B.; Berto, P.; Monneret, S.; Quidant, R.; Rigneault, H., Deterministic temperature shaping using plasmonic nanoparticle assemblies. *Nanoscale* **2014,** *6* (15), 8984-8989.
28. Landau, L. D.; Lifšic, E. M.; Pitaevskii, L. P., *Electrodynamics of continuous media*. Pergamon press: 1960; Vol. 364.
29. Baffou, G.; Rigneault, H., Femtosecond-pulsed optical heating of gold nanoparticles. *Physical Review B* **2011,** *84* (3), 035415.
30. Baffou, G.; Quidant, R.; Girard, C., Thermoplasmonics modeling: A Green's function approach. *Physical Review B* **2010,** *82* (16), 165424.
31. Baffou, G.; Bon, P.; Savatier, J.; Polleux, J.; Zhu, M.; Merlin, M.; Rigneault, H.; Monneret, S., Thermal Imaging of Nanostructures by Quantitative Optical Phase Analysis. *ACS Nano* **2012,** *6* (3), 2452-2458.
32. Berto, P.; Ureña, E. B.; Bon, P.; Quidant, R.; Rigneault, H.; Baffou, G., Quantitative absorption spectroscopy of nano-objects. *Physical Review B* **2012,** *86* (16), 165417.
33. Lal, S.; Hafner, J. H.; Halas, N. J.; Link, S.; Nordlander, P., Noble Metal Nanowires: From Plasmon Waveguides to Passive and Active Devices. *Accounts of Chemical Research* **2012,** *45* (11), 1887-1895.
34. Han, S.; Hong, S.; Ham, J.; Yeo, J.; Lee, J.; Kang, B.; Lee, P.; Kwon, J.; Lee, S. S.; Yang, M.-Y.; Ko, S. H., Flexible Electronics: Fast Plasmonic Laser Nanowelding for a Cu-Nanowire Percolation Network for Flexible Transparent Conductors and

Stretchable Electronics (Adv. Mater. 33/2014). *Advanced Materials* **2014,** *26* (33), 5888-5888.
35. Garnett, E. C.; Cai, W.; Cha, J. J.; Mahmood, F.; Connor, S. T.; Greyson Christoforo, M.; Cui, Y.; McGehee, M. D.; Brongersma, M. L., Self-limited plasmonic welding of silver nanowire junctions. *Nat Mater* **2012,** *11* (3), 241-249.
36. Verellen, N.; Van Dorpe, P.; Vercruysse, D.; Vandenbosch, G. A. E.; Moshchalkov, V. V., Dark and bright localized surface plasmons in nanocrosses. *Opt. Express* **2011,** *19* (12), 11034-11051.
37. Lee, J.-Y.; Connor, S. T.; Cui, Y.; Peumans, P., Solution-Processed Metal Nanowire Mesh Transparent Electrodes. *Nano Letters* **2008,** *8* (2), 689-692.
38. Song, T.-B.; Chen, Y.; Chung, C.-H.; Yang, Y.; Bob, B.; Duan, H.-S.; Li, G.; Tu, K.-N.; Huang, Y.; Yang, Y., Nanoscale Joule Heating and Electromigration Enhanced Ripening of Silver Nanowire Contacts. *ACS Nano* **2014,** *8* (3), 2804-2811.
39. Mickel, P. R.; Lohn, A. J.; James, C. D.; Marinella, M. J., Isothermal Switching and Detailed Filament Evolution in Memristive Systems. *Advanced Materials* **2014,** *26* (26), 4486-4490.
40. Kim, T.; Kim, Y. W.; Lee, H. S.; Kim, H.; Yang, W. S.; Suh, K. S., Uniformly Interconnected Silver-Nanowire Networks for Transparent Film Heaters. *Advanced Functional Materials* **2013,** *23* (10), 1250-1255.

Supplemental information

Quantitative study of the photothermal properties of metallic nanowire networks.

Alan P. Bell [†§⊥], Jessamyn A. Farifield [†§⊥], Eoin K. McCarthy[§], Shaun Mills [†§⊥], John J. Boland [†§⊥], Guillaume Baffou[‖], David McCloskey[‡§⊥]*

[†]School of Chemistry, Trinity College Dublin, Dublin 2, Ireland

[‡] School of Physics, Trinity College Dublin, Dublin 2, Ireland

[§] Centre for Research on Adaptive Nanostructures and Nanodevices (CRANN), Trinity College Dublin, Dublin 2, Ireland

[⊥] AMBER Research Centre, Trinity College Dublin, Dublin 2, Ireland

[‖] Institut Fresnel, CNRS, Aix Marseille Université, Centrale Marseille, UMR 7249,

13013 Marseille, France

The average nanowire length and diameter for each sample was determined using statistical analysis of TEM images. *Figure.S1* shows a representative image for (a) silver, (b) nickel and (c) gold. The silver nanowires have a 3 nm thick dielectric surface coating of poly(vinylpyrrolidone) (PVP) to avoid aggregation in solution, whereas the Ni wires have a 5 nm surface oxide layer.

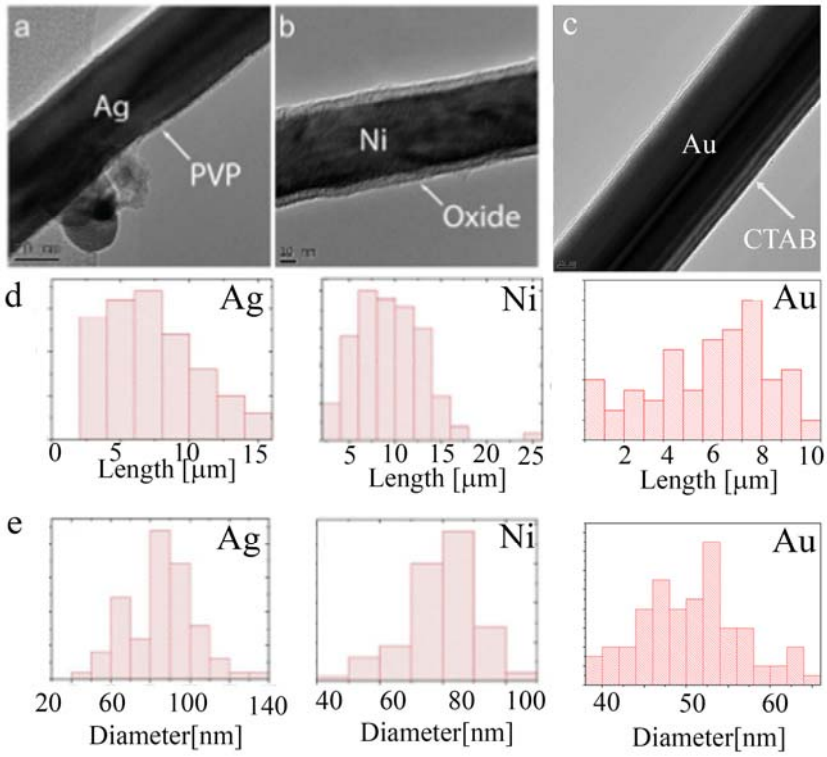

Figure S1. (a) TEM of single silver nanowire showing PVP layer. (b) TEM of nickel nanowire showing oxide layer (c-f) statistical size distributions of Nickel and silver nanowires taking from SEM imaging.

In this experiment the incident excitation was fixed at 532nm at the LSP resonance of the gold nanowires. It is clear however that the silver nanowires exhibited much lower absorption at this frequency. For applications using silver nanowires an excitation wavelength of 375 nm should be used. At this frequency the polarization contrast between absorption of TE and TM incident polarizations is maximum and larger than in gold or nickel nanowires. This shows that aligned

silver nanowires can be used as compact polarizers in the UV with an extinction of 16:1. This is shown in *Fig. S2* where the ratio of TE to TM absorption is plotted as a function of incident wavelength for Au, Ag and Ni nanowires.

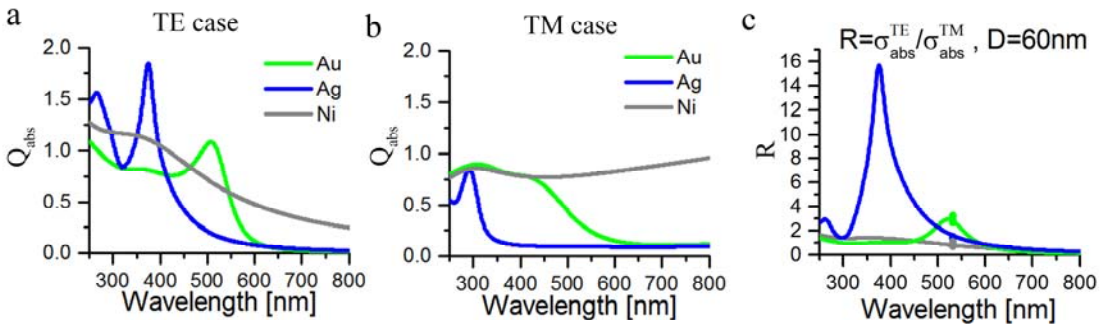

Figure S2: a. Frequency dependence of absorption efficiency for TE case. B. Frequency dependence for TM case. c. Ratio of heating $R = \sigma_{abs}^{TE} / \sigma_{abs}^{TM}$ for gold, silver and nickel nanowires. Experimental values at 532nm also shown as dots

Propagating surface plasmon modes can be excited at the finite end of a single nanowire. To study the contribution of theses modes to the total absorption cross section we conducted 3D FEM simulations. The intensity enhancement *Fig.S2a* and heat source density *Fig.S2c* for an 30nm radius infinite Ag wire, are compared with that of a semi-infinite wire with a 30nm radius spherical capped *Fig.S2c,d*. The relative heat source density is normalized to Mie theory for an infinite wire shows that the launched SPP modes contribute to increased heating in only the first 250 nm of the wire. The wire is in a symmetric environment (glycerol and glass with similar refractive index, so it is difficult to efficiently match the momentum required to launch a bound SPP mode in the nanowire. This sharp 250 nm falloff can be attributed to launching of lossy modes in the wire. The total contribution of SPPs to the absorption cross section can be seen by plotting the cumulative difference of the heating in the finite wire to that in an infinite in *Fig. S2f*.

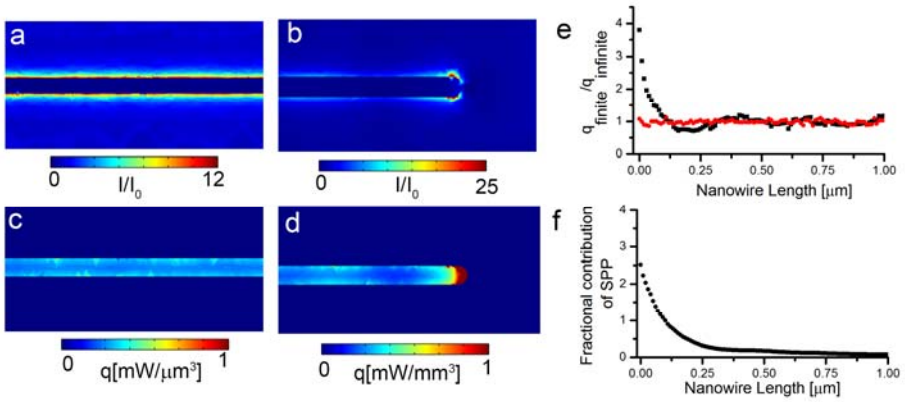

Figure S3: a Intensity enhancement for a single infinite 60nm diameter Ag wire excited at 532 nm. b. Intensity enhancement for a semi-infinite wire with same cross section. c Heat source density $q(\mathbf{r})$ for infinite wire. d $q(\mathbf{r})$ for finite wire. e Relative resistive heating for finte (black circles) and infinite (red circles) cases. f. Fractional contribution of SPPs to total absorption cross section as a function of nanowire length.

Measurements of temperature distributions and heat source densities were taken for multiple nanowires and junctions on each sample. For brevity only a few selected results were shown in the main text, however given the speed and simplicity of the technique a large number of nanowire samples were investigated. *Figure. S4* displays some additionally single wire heating results.

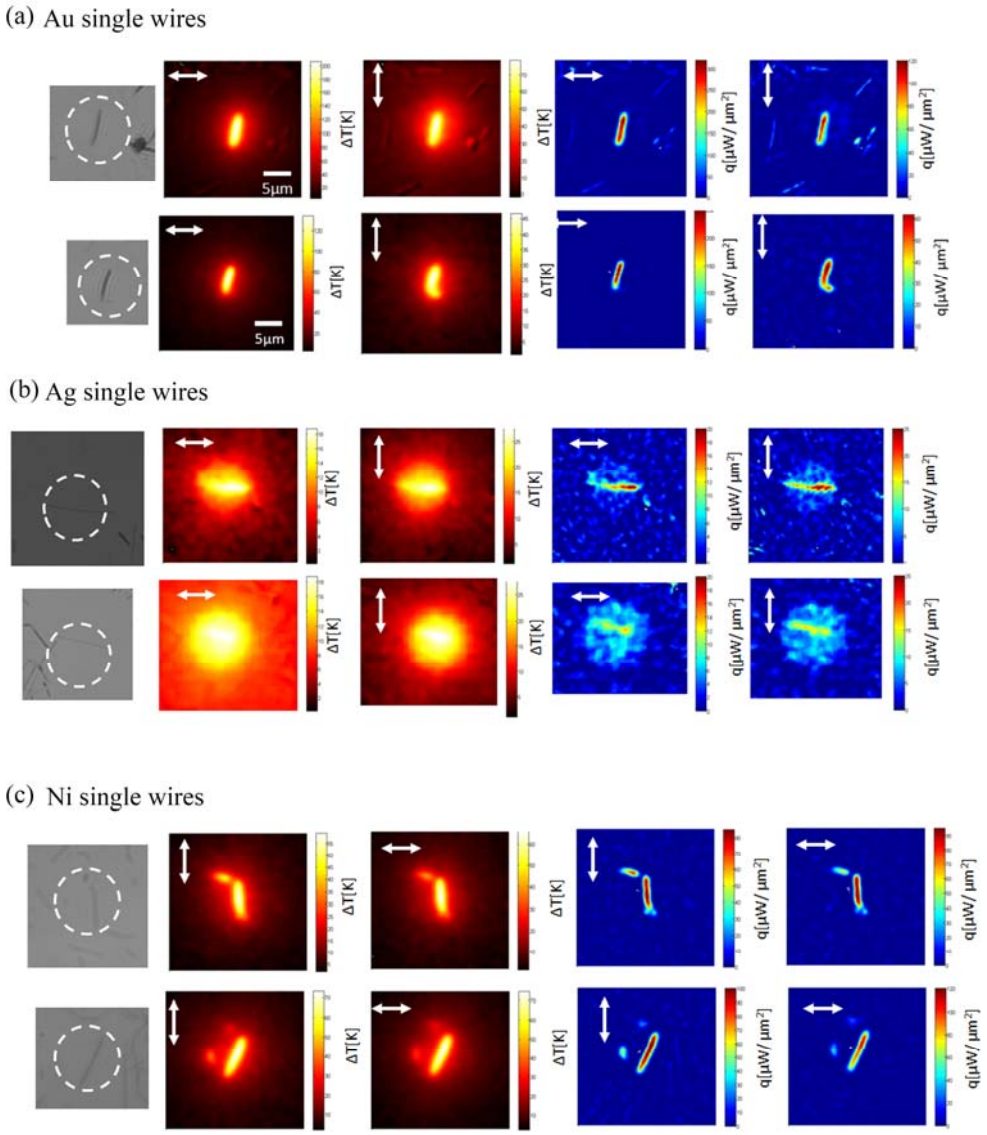

Figure S4: Experimental temperature distributions and heat source density maps for single nanowires. (a) Single Au nanowires with P_0=230mW and 133mW respectively. (b) Single Ag nanowires with incident power 230mW (c) Single Ni nanowires with incident power 147 mW.

Figure. S5 displays some additional experimental results for nanowire junctions

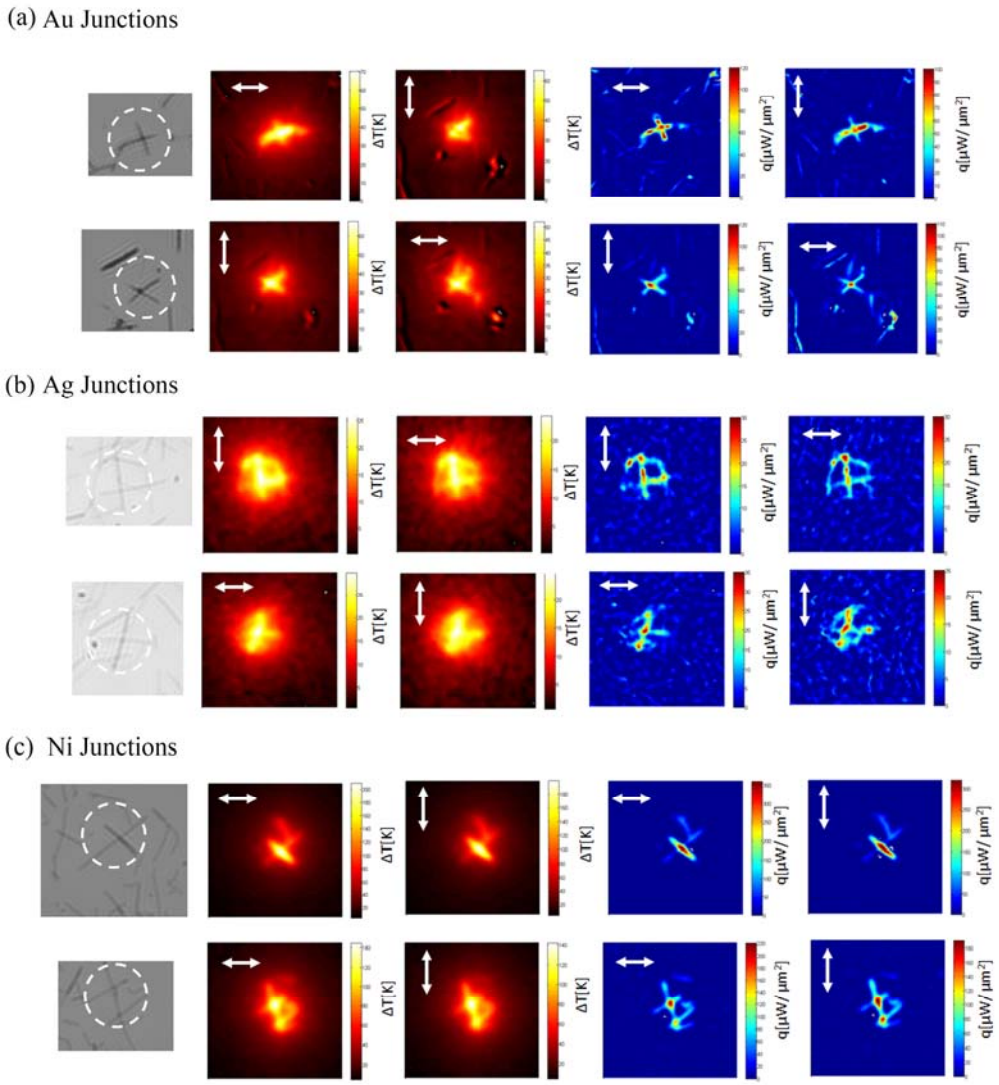

Figure.S5: Experimental temperature distributions and heat source density maps for crossed nanowires. (a) Au nanowire junctions with incident power P_0= 53 mW (b) Ag nanowire junctions with incident power P_0= 289 mW (c) Ni nanowire junctions with incident power P_0= 135 mW.

Electromagnetic and thermal finite element method simulations were performed using COMSOL MULTIPHYSICS^{TM} , commercially available software. Steady state temperature profiles taken 1nm above the layer surface are shown as a function of effective film thermal conductivity in Fig.

S6. The maximum temperature reached and slope of the falloff depend on the film thermal conductivity.

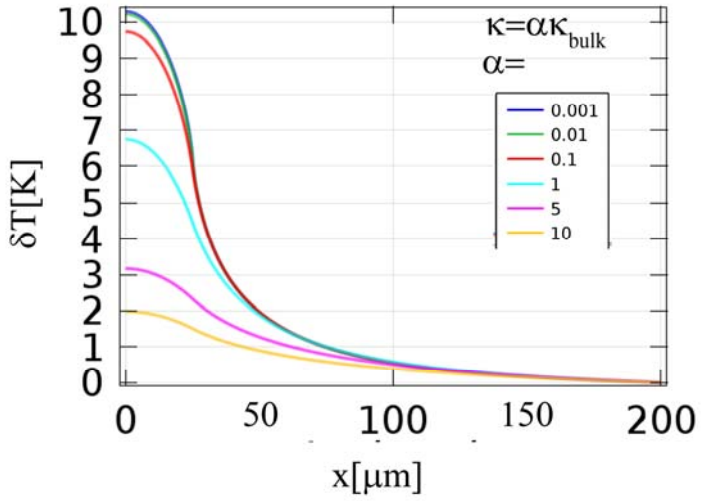

Figure.S6: FEM simulated radial dependence of steady state temperature rise for a 50 μm diameter illumination area as a function of effective film thermal conductivity.